

Statistical Strategy for Anisotropic Adventitia Modelling in IVUS

Debora Gil*, Aura Hernández, Oriol Rodríguez, Josepa Mauri, and Petia Radeva

Abstract—Vessel plaque assessment by analysis of intravascular ultrasound sequences is a useful tool for cardiac disease diagnosis and intervention. Manual detection of luminal (inner) and media-adventitia (external) vessel borders is the main activity of physicians in the process of lumen narrowing (plaque) quantification. Difficult definition of vessel border descriptors, as well as, shades, artifacts, and blurred signal response due to ultrasound physical properties trouble automated adventitia segmentation. In order to efficiently approach such a complex problem, we propose blending advanced anisotropic filtering operators and statistical classification techniques into a vessel border modelling strategy. Our systematic statistical analysis shows that the reported adventitia detection achieves an accuracy in the range of interobserver variability regardless of plaque nature, vessel geometry, and incomplete vessel borders.

Index Terms—Anisotropic processing, intravascular ultrasound (IVUS), vessel border segmentation, vessel structure classification.

I. INTRODUCTION

INTRAVASCULAR ultrasound (IVUS) imaging is a unique imaging clinical tool [1] that provides cardiologists with a cross-sectional inside view of the vessel [Fig. 1(a)] and, thus, allows a complete study of its morphology, such as arterial wall, lumen, or plaque. The technique helps diagnosis and treatment of cardiac diseases, as far as a precise characterization and segmentation of arterial structures are available. A manual processing of images, apart from being a tedious time consuming task, might suffer from intra- and interobserver variability. This fact motivates the development of image processing techniques addressing detection of arterial structures.

Since the middle 1990s, several algorithms for a reliable intima detection have been proposed [2]–[7]. By its inherent difficulty (its distance from the ultrasound transducer reduces sharpness in the border visual appearance), adventitia modelling has been only approached in recent work [8], [19]. However, an accurate border detection requires either elaborated strategies in

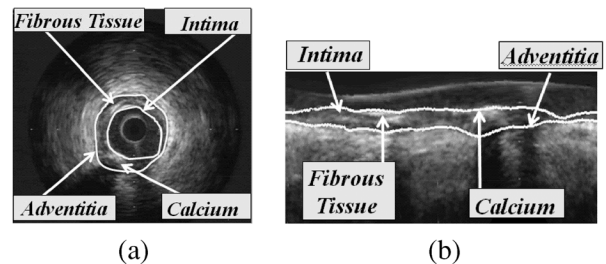


Fig. 1. IVUS images in (a) cartesian and (b) polar coordinates.

the case of contour-based segmentations [14]–[19], or a previous plaque and tissue characterization in the case of classification strategies [12], [13]. In the presented work, we describe an adventitia detection method based on a supervised learning of the boundary descriptors followed by a segmentation determined by its geometry.

Usual techniques addressing segmentation of vessel borders (intima and adventitia) rely on a single local image descriptor (usually edges). Energy minimization contour-based techniques either guide a snake towards the target structures [14]–[19], or minimize a cost function [2]–[4]. Regardless of low quality in IVUS images, adventitia detection adds the difficulty of a large variety of descriptors, a weak visual appearance by a decrease in the ultrasonic pulse energy [22], and incomplete contours due to echo opaque plaques (e.g., calcium) shadowing. It follows that standard segmentation approaches do not suffice by their own and need ad hoc strategies to yield proper results. Some authors [2]–[4], [18], [19] combine transversal and longitudinal contours to endow the model with spatial continuity along the sequence. In this case, the use of electrocardiogram (ECG)-gated sequences [4] significantly helps to achieve a reliable segmentation of longitudinal cuts. Other approaches [5], [6], [8] manually restrict a region of interest that serves to initialize a snake, although such initialization might need to be updated along the sequence.

A common inconvenience of segmentation based on contour detection is that it requires some kind of image filtering to avoid fake responses. The poor image quality as well as large variety of IVUS artifacts (calcium, shadows, catheter guide and blood back scatter) make standard anisotropic smoothing [31] fail to achieve optimal results. In order to overcome these drawbacks, several approaches have been proposed. A straightforward strategy is to discard those images containing too many artifacts [14]. More elaborated approaches [7], [21] directly handle raw data and filter impulse responses of the transducer. Unfortunately, raw data acquisition needs a special device not always available in standard clinical equipments.

Manuscript received November 21, 2005; revised March 10, 2006. This work was supported in part by the “Fundació Caixa Sabadell” and in part by the Ministerio de Ciencia y Tecnología of Spain under Project FIS-G03/1085, Project FIS-PI031488, and Project TIC2003-00654. *Asterisk indicates corresponding author.*

*D. Gil is with the with the Computer Science Department, Computer Vision Center, Universidad Autonoma de Barcelona, Barcelona 08193, Spain (e-mail:debora@cvc.uab.es; debora@cnb.uam.es).

A. Hernández, and P. Radeva are with the Computer Science Department, Computer Vision Center, Universidad Autonoma de Barcelona, Barcelona 08193, Spain.

O. Rodríguez, and J. Mauri with the Unitat d’Hemodinàmica Cardíaca i Cardiologia Intervencionista, Servei de Cardiologia, Hospital Universitari Germans Trias i Pujol, Crta Canyet s/n 08916 Badalona.

Digital Object Identifier 10.1109/TMI.2006.874962

Recent approaches [7]–[13], [23] use either a probabilistic framework [7]–[9] or classification strategies [10]–[13], [23] to better characterize coronary structures (plaque and vessel borders). Although results are robust to noise and artifacts, some of them [8], [12], [23] require a manually delineated region of interest [8], [12] or an accurate segmentation of the first sequence frame for each different case [23].

IVUS processing methods base, so far, on either image gray-value changes or exhaustive classification of image structures. We argue that in order to obtain a robust detection of vessel borders, both strategies should be combined. Boundary detection in general complex images (not necessarily IVUS) should hinge on more than one image descriptor [23], [26], [35] and take into account level sets geometry [26], [28]. The latest advances in the field [23], [26], [35] suggest the use of supervised classification techniques in order to learn the values that best characterize the boundary of interest. The statistical strategy for anisotropic adventitia detection we propose is a three-fold algorithm that combines supervised learning with geometric-based filtering and segmentation techniques. In a first preprocessing step, a restricted anisotropic diffusion (RAD) [29] sharpens vessel borders appearance in the polar transform of each IVUS frame. In the second stage, supervised classification techniques serve to compute two binary maps: one for vessel borders and another one for calcium sectors. The latter is used to discard sectors of ambiguous information due to echo shadowing [calcium plaque in Fig. 1(a)]. In the last step, the fragmented vessel segments of the vessel mask are modelled by computing an implicit closed representation using an anisotropic contour closing (ACC) [28] and, then, an explicit B-spline compact parameterization.

The topics are presented as follows. In Section II, we outline the main steps of the algorithm. Image preprocessing and the selection stage are detailed in Sections III and IV, and computation of a closed model in Section V. Sections VI and VII are devoted to validation of the method and Sections VIII and IX to discussion, conclusions, and further research.

II. GENERAL STRATEGY

The strategy for media-adventitia (simply adventitia from now on) segmentation we suggest summarizes in the following three main steps:

STEP I. Image Preprocessing:

- 1) Polar Transformation of IVUS images—Advanced techniques for medical imaging segmentation use *a priori* knowledge of the target structure shape [26]. In the case of the adventitia border, its circular-like appearance is taken into account by transforming images to polar coordinates with the origin at the geometric center of the vessel border. In this coordinate system, the adventitia is nearly a horizontal curve, which significantly simplifies border feature extraction and parameterization.
- 2) RAD—In order to enhance significant structures while removing noise and textured tissue, we use an RAD [29]. This filtering scheme modifies classic anisotropic diffusions [31] by suppressing any diffusion across image level curves. The associated image operator homogenizes image

structures gray values according to their geometric continuity and, thus, results in a more uniform response to image local descriptors (edges, valleys, ridges).

STEP II. Border Points Features Learning: The goal of the selection stage is to compute a mask of vessel border segments and calcium sectors. Extracting vessel borders and calcium points requires defining the functions that best characterize each set, as well as their most discriminating parameter values. We learn both feature space and parametric threshold values by applying supervised classification techniques to a training set of manually segmented images.

- 1) Feature Space Design—Our feature space is designed to discriminate among the set adventitia/intima, calcium, and fibrous tissue. Calcium sectors are discarded by their shadowing of tissue and adventitia. Fibrous tissue is discriminated by its similar appearance to vessel borders [Fig. 1(a)]. By the polar coordinates chosen [Fig. 1(b)], horizontal edges are the main descriptors of the set adventitia/intima. Image simple statistics serve to formulate the functions characterizing calcium and fibrous plaque.
- 2) Parameters Determination—In our segmentation procedure, there are two kinds of parameters, those that best discriminate among different structures in the feature space and those controlling filtering of fake responses. Discriminating parameters are thresholding values on the feature space, while length filtering removes spurious detections from the extracted segments. Both parameters are tuned to yield an optimal segmentation for a training set of manually traced borders.

STEP III. Segmentation Stage: The selection stage produces two binary images: adventitia/intima points and calcium sectors. Vessel border segments are modelled by computing an implicit closed representation and, then, an explicit snake representation using B-splines.

- 1) Implicit ACC—For the implicit closing, we suggest using an ACC [28] based on functional extension principles to complete curve segments in the image mask domain. The use of restricted diffusion operators enables to take into account image geometry, restore curved shapes, and discard calcium and side branch sectors. We endow three-dimensional (3-D) continuity to such implicit reconstruction by topological area considerations.
- 2) Explicit B-Snakes Representation—We define vessel contours at uncomplete segments (e.g., branches or calcification) by approaching ACC with a B-spline snake encoded with N control points.

III. PREPROCESSING

A. Polar Coordinates

From now on, we will work with images in polar coordinates (Fig. 2), namely $\text{AdvPol}(i, j)$. Rows $i = 1, \dots, \min(Nc, Nr)$ (for Nc, Nr the columns and rows of the original IVUS image) represent the radius R and columns $j = 1, \dots, 360$ the angle θ . We reserve indexes i, j for the discrete sampling of a continuous image given in positively oriented x, y axes.

In an IVUS plane, the adventitia border is an elliptic-like shape with a relatively small eccentricity [Fig. 1(a)]. In polar

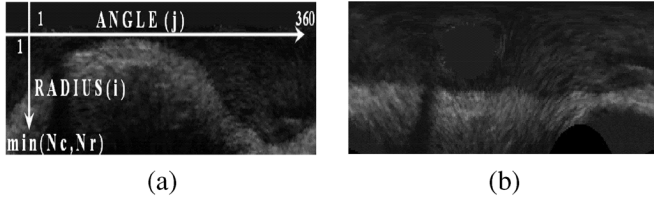


Fig. 2. Image center versus adventitia center. (a) Polar images with origin at the image center and (b) at the adventitia geometric center.

coordinates with the origin at the border geometric center, the adventitia converts into a nearly horizontal line that can be parameterized by the radius. The lumen geometric center does not coincide with the ultrasound probe (image center) and has to be computed (see [20] for a detailed explanation). The computation of the adventitia geometric center is twofold: first we suppress the lumen displacement in the image due to heart dynamics and then we compute the geometric center of the static vessel.

Vessel translation induced by heart motion is reduced by taking as origin the image mass center as its spatio-temporal evolution captures cardiac motion. Still, in such polar systems [Fig. 2(a)], the adventitia might present a static curved pattern if the vessel is not centered at such mass center (e.g., in the presence of calcium). This geometric curvature is reduced by computing the geometric center of a set of points roughly lying on the adventitia. Such points are extracted by using the statistical strategy (see Section IV-B and [20]) used to compute the adventitia/intima mask.

Fig. 2 illustrates the main steps of the geometric eccentricity suppression. Fig. 2(a) shows the polar transform with the origin at the image mass center with the usual undulation produced by an origin different from the vessel geometric center. The straightened adventitia image [Fig. 2(b)] has the catheter appearing at the center of the lumen in the second quartile of the image by its deviation from the geometric center.

B. RAD

Most filtering techniques based on image gray level modification [31] use the heat diffusion equation

$$I_t(x, y, t) = \text{div}(J\nabla I)I(x, y, 0) = I_0(x, y) \quad (1)$$

to denoise an image $I_0(x, y)$. The time dependent function I is the family of smoothed images and J is a two-dimensional (2-D) metric (i.e., an ellipse) that locally describes the way gray levels redistribute. The diffusion tensor J is thoroughly described by means of its eigenvectors $(\xi, \eta = \xi^\perp)$ and eigenvalues (λ_1, λ_2) . If the latter are strictly positive, like in existing anisotropic filtering techniques [30], [31], gray values spread on the whole image plane and the time evolution of I_0 converges to a constant image. But if we degenerate J and admit null eigenvalues $(\lambda_2 = 0)$, then diffusion only takes place in the integral curves of the eigenvector (ξ) of positive eigenvalue [28]. Smoothing effects depend on the suitable choice of the eigenvector of positive eigenvalue. In the case that ξ is a smooth vector representing the tangent space to a closed model of the image level sets, then the final image is a collection of curves of uniform gray level [29].

The structure tensor [34] is a quick way of computing the guiding vector ξ that has already proven its efficiency [28]. The structure tensor, namely ST_ρ , is a Gaussian mean of the projection matrices onto a regularized image gradient. That is, given a Gaussian G_ρ of variance ρ and zero-mean, the structure tensor is the following convolution:

$$\text{ST}_\rho = G_\rho * \left[\begin{pmatrix} I_x \\ I_y \end{pmatrix} (I_x, I_y) \right] = \begin{pmatrix} G_\rho * I_x^2 & G_\rho * I_x I_y \\ G_\rho * I_x I_y & G_\rho * I_y^2 \end{pmatrix}$$

for $(I_x, I_y) = G_\sigma * \nabla I$ the components of a regularized image gradient. The eigenvectors of the structure tensor represent a smooth extension of the image level sets tangent space [28]. The scale σ controls the degree of Gaussian image smoothing used to compute the initial tangent space and ρ the scope of the extension of such space. In order to preserve the detail in the continuous curves of the image, we recommend keeping σ as low as possible ($\sigma = 0.5$ in a discrete implementation). As for the extension scale ρ , we have experimentally checked (with more than 400 images ranging from natural scenes [28] to medical imaging [19]) that the range $\rho \in [1, 2]$ achieves a good compromise between restoring closed models of continuous curves and keeping the random nature of texture and noise.

We use ST_ρ eigenvectors to design our diffusion tensor as follows. Let us consider a metric \tilde{J} with eigenvalues $\lambda_1 = 1$ and $\lambda_2 = 0$, and ξ the eigenvector of minimum eigenvalue of ST_ρ . The restricted heat diffusion we suggest is given by

$$I_t = \text{div}(Q\tilde{\Lambda}Q^t\nabla I), I(x, y, 0) = I_0(x, y) \quad (2)$$

with Q given by the eigenvectors of

$$\text{ST}_\rho = G_\rho * (\nabla I_\sigma \nabla I_\sigma^T)$$

and

$$\tilde{\Lambda} = \begin{pmatrix} 1 & 0 \\ 0 & 0 \end{pmatrix}, \quad \nabla I_\sigma = G_\sigma.$$

Since the guiding vector ξ is oriented along image structures and randomly at textured and noisy areas, RAD smoothes image gray values along its regular structures and acts like a Gaussian filter otherwise. The result is that solutions to (2) converge to a smooth image that has a uniform continuous response to standard detectors based on the image local descriptors. Fig. 3 illustrates the mechanisms and effects of (2) in a calcified region (first column) and near the intima and a fibrous tissue (second column). We applied a standard ridge detector to the calcium image and a horizontal edge operator to the intima/fibrous tissue one. The vector ξ depicted in Fig. 3(a) and (b) is well defined near the structures and randomly distributed in textured tissue [Fig. 3(b)] and the echo opaque shadow below calcium [Fig. 3(a)]. The original response [Fig. 3(c) and (d)] yields fragmented curves for the target structures and fake detections due to noise. In RAD images [Fig. 3(e) and (f)], background spurious edges [Fig. 3(f)] have been removed, while the intima, the fibrous structure, and calcium are regular curves with a minimum fragmentation.

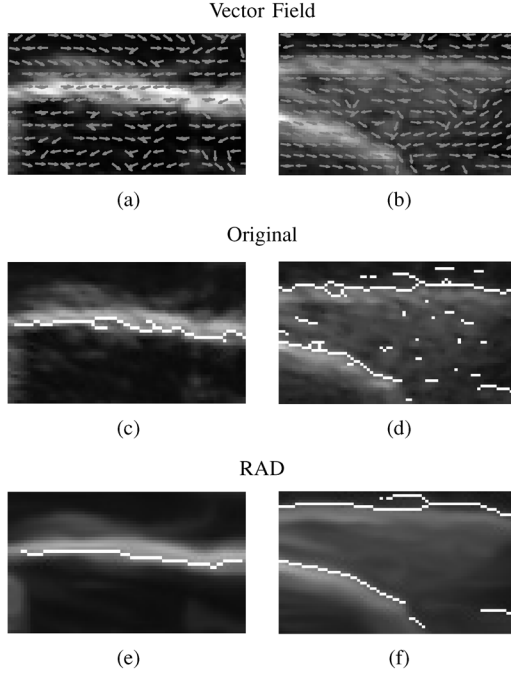


Fig. 3. RAD smoothing for calcium (first column) and adventitia (second column).

IV. STATISTICAL SELECTION OF BORDER POINTS

The inner and outer vessel borders' appearances are so similar that they are assumed to constitute a single class in the training process. Their distinct radial position suffices to discriminate them [19] in the absence of echo opaque structures, such as calcium. In such cases, the adventitia does not appear and the detection is misled towards the intima. The best solution is to discard echo opaque (calcium) sectors, so that the training stage also addresses their characterization. Fibrous tissue discrimination is also included because it is a main artifact confused with the adventitia pattern (see Fig. 1), especially in complex plaques.

A. Feature Space Design

The feature space is a 3-D space tuned to describe the adventitia/intima and echo opaque structures.

- 1) *Horizontal Edges*: Since in the coordinate system chosen, the adventitia layer is a horizontal dark line, horizontal edges constitute our main descriptor. Edges are computed by convolving the image with the y -partial derivative of a 2-D Gaussian kernel of variance $\sigma = 0.5$, in order to keep the maximum accuracy in edges location.

The only structures yielding large values for e_y are intima, adventitia, calcium, and fibrous tissue. Intima and adventitia correspond to negative values, while calcium and fibrous structures yield a negative and a positive response, one for each of their bordering sides. The descriptors we have chosen to detect echo opaque plaques and fibrous tissue are their outstanding brightness and, for calcium, the dark shadow underneath.

- 2) *Radial Standard Deviation*: Striking brightness corresponds to an outlier of the pixel gray value in the radial direction. We measure it by means of the difference between the pixel gray value and the radial mean. For each

pixel (i, j) , we define

$$\sigma(i, j) = (\text{AdvPol}(i, j) - \mu(j))^2$$

where $\mu(j)$ is the radial (i.e., column-wise) mean of the polar image

$$\mu(j) = \frac{1}{N_r} \sum_{i=1}^{i=N_r} \text{AdvPol}(i, j).$$

The magnitude of σ is maximum at bright structures (calcium and fibrous plaque) and close to zero near the adventitia. In order to distinguish between calcium and fibrous plaque, we add the following shadows detector.

- 3) *Radial Cumulative Mean*: For each column j , consider the following cumulative mean:

$$\tilde{\nu}_j(i) = \frac{\sum_{n=R_{\max}}^{n=i} \text{AdvPol}(n, j)}{R_{\max} - i}.$$

For angles with calcium, the function $\tilde{\nu}_j(i)$ presents a step-wise profile in contrast to a more uniform response in the presence of fibrous plaque. Due to the shadowing effect, the total radial energy

$$\epsilon(j) = \sum_{i=1}^{i=R_{\max}} \tilde{\nu}_j(i)$$

achieves its minimum values at sectors with calcium.

The feature space achieving a maximum separability for our training set is given by

$$(X, Y, Z) = (e_y, \text{sign}(e_y) \sqrt{|e_y \sigma|}, \epsilon).$$

B. Statistical Parameter Setting

For the computation of the vessel borders and calcium binary images, the classification problem we must face is discriminating among four different sets: adventitia/intima (Adv), calcium (Cal), fibrous structures (Fbr), and the rest of pixels (RP). Instead of addressing the four-class problem as a whole, we will solve several binary problems in two dimensions: first we discriminate between $C_1 = (\text{Adv}, \text{RP})$ and $C_2 = (\text{Cal}, \text{Fbr})$, and then we separate the two classes within each of the sets.

For its simplicity and proven efficient performance, our main classifying tool will be Fisher linear discriminant analysis [32]. Linear discriminant analysis searches for the linear subspace W that achieves a maximum separability among the projected classes. Mathematically, this criterion is formulated in terms of the ratio between the between-class S_B and the within-class S_W scatter matrices

$$S_B = \sum_{i=1}^c (\mu_i - \mu)(\mu_i - \mu)^t$$

$$S_W = \sum_{i=1}^c \sum_{j=1}^{N_i} (\mathbf{Y}_j - \mu_i)(\mathbf{Y}_j - \mu_i)^t$$

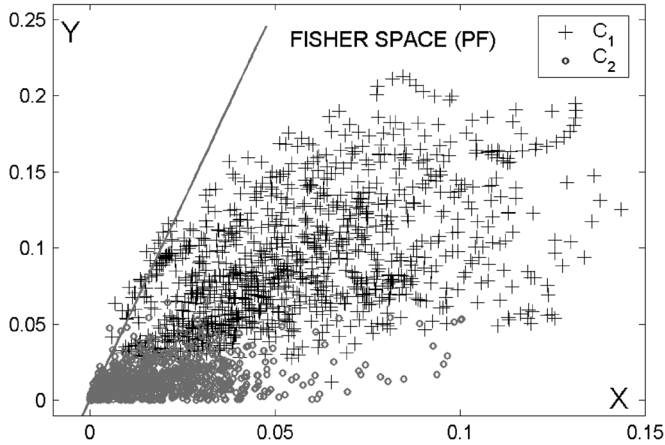


Fig. 4. Discrimination between C_2 and C_1 in the $X/e_y - Y/\sigma$ feature Space.

for c the number of classes, N_i the samples per class, μ_i the mean vector of each of them, and μ the mean of all samples (Y_j). Fisher criterion for W is maximizing

$$J(W) = \frac{|W^t S_B W|}{|W^t S_W W|}.$$

In the particular case of a two-class problem in two dimensions, Fisher space is a straight line (solid line in Fig. 4) and discrimination between the two classes is achieved by a threshold on the projection space.

We use a Bayesian approach [32] to select thresholding values in terms of missclassification errors. In the two-class problem, Bayes searches for the value that achieves a suitable compromise between the percentage of false positives and false negatives. The approach selects a threshold in terms of how many true positives are detected without considering the amount of noise introduced in the positive detections. Although the criterion is widely used in classification problems, in the case of severe unbalanced classes or object segmentation [35], it is more efficient to select thresholds in terms of the tradeoff between precision and recall.

1) *Vessel Borders Mask*: Borders extraction is achieved by addressing two classification issues: discriminate $C_1 = (\text{Adv}, \text{RP})$ and $C_2 = (\text{Cal}, \text{Fbr})$ in the (X, Y) plane, and then, separate Adv from RP using X values.

We discriminate C_1 (positives) and C_2 (negatives) by projecting onto the Fisher space $PF1$ (see Fig. 4) and tuning the standard Bayesian threshold. Since our discriminating problem is detecting as much adventitia points as possible, we select the value τ_{PF1} that, among all thresholds ensuring at least 90% of C_1 detections, yields optimal segmentation results. Discrimination between Adv and RP is achieved in the X coordinate domain, as Adv corresponds to large negative values. A large range of Adv values among different patients suggests the use of an image-sensitive threshold rather than a common value for all cases. We adopt a strategy in the fashion of discriminant snakes [23], [24] and select a different value for each column. Radial (column-wise) percentiles (ρ_X) are used to compute such threshold. Finally, small structures in the vessel borders image

are removed by applying a length filtering, so that only segments of length above a given percentile (ρ_L) are kept.

If we note by $PF1$ the projection of the (X, Y) space onto the Fisher line, then, for every frame, points are labelled as Adv if they fulfill

$$PF1 < \tau_{PF1}, X < \rho_X$$

and their segment length is above ρ_L . Fig. 5(b) and (c) illustrates the extraction of adventitia/intima points. In Fig. 5(b), we have the output of the discrimination step, and in Fig. 5(c), the result after applying a length filtering.

2) *Calcium Mask*: Because calcium sectors are discarded and fibrous tissue might be close to the adventitia border, the latter must be removed from the calcium mask. The feature space chosen to discriminate calcium from fibrous tissue is given by the projection $PF1$ and the Z coordinate. A threshold on the Fisher space $PF2$ for the 2-D space $(PF1, Z)$ separates Cal and Fbr. Instead of following a Bayesian approach, we will follow a precision-recall criterion and among all thresholds admitting, at most, 10% of noise, we select the value τ_{PF2} that ensures a better segmentation of our training set.

It follows that calcium points are those pixels that satisfy

$$PF1 \geq \tau_{PF1} \text{ and } PF2 > \tau_{PF2}.$$

V. CLOSING STAGE

The selection stage produces two mask (binary) images: one for calcium [Fig. 5(a)] and another one for vessel borders [Fig. 5(c)]. In the case of noncircular patterns (caused by either catheter tilting or vascular modelling in eccentric plaques), the adventitia mask might result in a sparse collection of fragmented curve segments which omits the most curved sectors of the border. In order to correctly restore the vessel geometry, we use a geometric contour closing [28] and then a B-snake modelling to recover a smooth representation.

A. Implicit ACC

Heat diffusion has the property of smoothly extending a function defined on a curve in the plane, provided that boundary conditions are changed to Dirichlet [33]. By using restricted heat operators, this property can be used to complete unconnected contours [28] as follows. Let γ be the set of points to connect, χ_γ its characteristic function (a mask), and define \tilde{J} as in RAD (2), then the extension process

$$u_t = \text{div}(\tilde{J}\nabla u), \quad \text{with } u|_\gamma = u_0 \quad (3)$$

converges to a close model of γ . Intuitively, we are integrating the vector field ξ , that is, we are interpolating the unconnected curve segments along it. For adventitia completion, the vector ξ is the eigenvector of minimum eigenvalue of the structure tensor computed over the edge map e_y . Wrong continuations at side

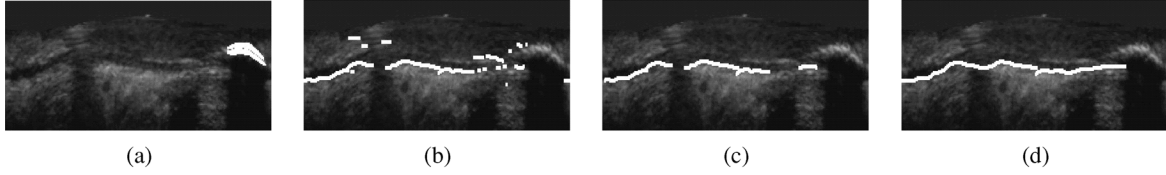


Fig. 5. Vessel Borders Extraction: (a) calcium mask, (b) adventitia mask from the classification, (c) adventitia mask after length filtering, and (d) ACC.

branches, sensor shadows, and calcium sectors are avoided by weighting the vector ξ with

$$w_{\xi}(i, j) = \begin{cases} 0, & \text{if } (i, j) \in \text{Calcium} \\ \text{coh} = \frac{(\lambda_1 - \lambda_2)^2}{(\lambda_1 + \lambda_2)^2}, & \text{otherwise} \end{cases}$$

for $\lambda_1, \lambda_2, \text{ST}_{\rho}$ eigenvalues with $\lambda_1 \geq \lambda_2$. At regions where ξ is a continuous vector, λ_2 is close to zero, so coh is maximum. Meanwhile, at noisy areas, since ξ is randomly oriented, λ_1 compares to λ_2 and $\text{coh} \sim 0$. This avoids missinterpolations at side branches and underneath the guide wire.

Because the classification used to select points on the border does not provide us with an exhaustive discrimination among all image structures, ACC closure might contain sparse segments that do not correspond to vessel borders (part of the guide, external fibrous tissue, etc.). Such artifacts do not vary continuously along the sequence and are removed by applying a filtering on the surface given by blocks of N consecutive ACC closings. That is, only connected components with an area above a given threshold are preserved.

B. B-Snake Representation

Although ACC closure already contains all available information, by the discrete implementation used, the implicit model is an irregular step-wise model that still presents gaps at side branches and calcium sectors. Moreover, we are motivated in guiding a parametric B-snake towards ACC closure to obtain a compact smooth explicit representation. A parametric snake is a curve $\gamma(u) = (x(u), y(u))$ which, under the influence of an external force E_{ext} and internal constraints E_{int} , minimizes an energy functional. In polar coordinates, as the adventitia is convex, we have that $\gamma = (\theta(u), R(u))$ can be represented as a function of the angle $R = R(\theta)$ so that the snake functional is defined as

$$E(R(\theta)) = \int_1^{360} (\alpha \|R_{\theta}\|^2 + \beta \|R_{\theta\theta}\|^2 + (R - R_{\tau})^2) d\theta$$

for R_{τ} the radius of the target curve and $R_{\theta}, R_{\theta\theta}$ the first and second derivatives of the radius. If we parameterize with a B-spline given by N control points

$$R(\theta(s)) = R(s) = \sum_i c_i(s) R_i, \quad \text{for } s \in [0, N-1] \quad (4)$$

the functional (4) converts to a function of the N control points, with the minimum defined by

$$\frac{\partial E}{\partial R_j} = 0, \forall j \in \{1, \dots, N\}. \quad (5)$$

Since the j th equation is

$$\left(\frac{2\alpha}{\lambda^2}\right) \sum_i \left(\int \dot{c}_j \dot{c}_i\right) R_i + \left(\frac{2\beta}{\lambda^4}\right) \sum_i \left(\int \ddot{c}_j \ddot{c}_i\right) R_i + \sum_i \left(\int c_j c_i\right) R_i = \int c_j R_{\tau} \quad (6)$$

for $\lambda = d\theta/ds = \theta_s$, the system (4) admits a matrix formulation given by

$$(B_1 + B_2 + B_0)R = BR = F_{\tau}. \quad (7)$$

The entries of B_j are sums of the j th derivatives of the spline coefficients c_i . The term $(B_1 + B_2)$ corresponds to the stiffness matrix for B-splines snakes and B_0 is the extra term coming from our particular external energy. The forces F_{τ} induced by the target curve are computed via the parameter change $R_{\tau}(\theta(s))$, for $\theta(s) = \sum_i c_i(s)\theta_i$.

If the target radius is defined, for each angle, as the maximum radius along the i -essim column corresponding to such angle, then the solution to (7) is given (as in [23]) by $R = B^{-1}F_{\tau}$. The cartesian transform of the polar spline given by the above radial control points is our final adventitia model.

VI. VALIDATION PROTOCOL

A. Study Group

We have validated our strategy in sequences captured with a Boston Scientific Clear View Ultra scanner at 40 MHz with constant pull-back at 0.5 mm/s and a digitalization rate of 25 frames/s. The digitalized sequences are 384×288 images with a spatial resolution of 0.0435 mm per pixel. The study group has been designed to assess the ability of the reported algorithm to detect the adventitia border in the presence of different plaques, artifacts, and vessel geometries. A total number of 5400 images extracted from 11 different cases has been tested. The sequences analyzed are clinical cases of the Hospital Universitari ‘‘Germans Trias i Pujol’’ in Badalona, Spain. We have segmented 22 vessel segments of a length ranging from 4 to 6 mm (200–300 frames) with the following clinical record:

- The population is 90% male and 10% female subjects between 36 and 76 years old.
- The segments are: 7 right coronary, 4 circumflex, 9 left anterior descending, and 2 left main segments.
- The cases include 6 stable and 2 unstable angina and 3 postmyocardial infarctions. Half of the cases were subject to stent placement and a 25% to angioplasty.
- Segments include incomplete vessel borders, calcified and noncalcified plaques, and normal segments.

Stented segments have been excluded because some designs may obscure the external elastic membrane border and render measurements unreliable [37]. For each segment, the adventitia has been manually traced every ten frames by four experts in IVUS image interpretation, which yields a total number of 540 validated frames with four different manual models each. The manual tracing was performed by showing the whole sequences to experts and interactively stopping every ten frames.

B. Accuracy Measures

To assess the segmentation accuracy, the automatically detected borders have been compared to the manual models. Accuracy is quantified with the following standard measures:

1) *Absolute and Signed Distances*: Distance maps serve to compute the difference in position between automatic and manually traced curves. Such maps encode for each pixel $p = (x_p, y_p)$ its distance to the closest point on the manual contour

$$D(p) = \min_{q \in \gamma} \left(\sqrt{(x_p - x_q)^2 + (y_p - y_q)^2} \right) \quad (8)$$

where q are points on the manually identified contour. Signed distances (SgnD) [27] weight the value $D(p)$ depending on whether the pixel p lies inside or outside the target curve γ . Its mean value detects any bias in curve position, that is, whether detections are systematically bigger or smaller than manual segmentations.

We consider absolute (in millimeters) and relative (in percent) distance errors. Absolute errors are given by formula (8), while relative ones are the ratio: $\text{RelD}(p) = 100 \cdot (D(p))/(d(q, O))$, for the origin O the mass center of the manual contour and q the point achieving the minimum in (8). Since relative errors consider the vessel true dimensions, they reflect positioning errors better.

For each distance error, its maximum and mean values on the automated contour are the error measures used to assess position accuracy. If PixSze denotes the image spatial resolution and p is any point on the automatically traced adventitia, then the set of functions measuring accuracy in positions are:

- **Maximum distance errors** (in millimeters and percent):

$$\begin{aligned} \text{MaxD} &= \max_p(D(p) \cdot \text{PixSze}) \\ \text{RMaxD} &= \max_p(\text{RelD}(p)) \end{aligned}$$

- **Mean distance errors** (in millimeters and percent):

$$\begin{aligned} \text{MD} &= \text{mean}_p(D(p) \cdot \text{PixSze}) \\ \text{RMD} &= \text{mean}_p(\text{RelD}(p)) \end{aligned}$$

- **Mean signed distance error** (in millimeters):

$$\text{MSD} = \text{mean}_p(\text{SgnD}(p) \cdot \text{PixSze}).$$

B) *Area Differences*: Binary images of manual $I_M(i, j)$ and automatic $I_A(i, j)$ borders serve to compute the following measure for area accuracy:

- **Percentage of Area Differences**

$$\text{AD} = 100 \cdot \frac{\sum_{i,j} |I_M(i, j) - I_A(i, j)|}{\sum_{i,j} I_M(i, j)}.$$

The interval given by the mean \pm standard deviation computed over the four expert contours indicates the statistical range of values for each of the automated errors (MaxD, RMaxD, MD, RMD, and AD). However, accuracy in models strongly depends on the pixel resolution as well as on the (manual) visual identification of the adventitia layer. The first consequence hinders any comparison to other segmentation algorithms as the minimum error (in millimeters) depends on pixel precision. The second one implies that an analysis of automated errors might not reflect, by its own, the true accuracy of segmentations, since a large variation range might be caused by a significant difference among expert models. A standard way [36] of overcoming the above phenomena is by comparing by T-test automated errors to the variability among different manual segmentations (inter-observer variability).

VII. RESULTS

The set of the optimal parameters is given by

$$PF1 = 0.1906X + 0.9817Y$$

with

$$\tau_{PF1} = 0.0619; \quad \rho_X = 6\%; \quad \rho_L = 80\%$$

for computation of vessel borders mask and

$$PF2 = -0.1498PF1 + 0.9887Z, \tau_{PF2} = 0.1295$$

for the calcium mask. The training cases are a randomly sampled set (810 frames) representing 30% of half of the available population. The adventitia detection parameters ensure 99.95% of true C_1 detections with just 6% of fake detections. In the case of calcium extraction, the threshold achieves less than 1% of noise and ensures 99.96% of calcium detections. The B-snake model uses 30 control points uniformly placed every 12 angles.

Some of the segmentations achieved with the presented strategy are shown in Fig. 6, column (A). corresponds to images with calcified plaque. Images in Fig. 6, column (B) have been extracted from noncalcified vessel segments, nonfibrous plaques in the first two images, and a normal segment in the last one. Finally, images with missing information are shown in Fig. 6, column (C), sensor guide shadows in the first two and side branches in the last one.

A. Statistics

Fig. 7 shows whisker boxes for mean distance absolute errors [Fig. 7(a)] and mean interobserver variations [Fig. 7(b)] for a representative sample of soft plaque and calcium segments. Each box contains the mean distance errors obtained from the four expert segmentations (80–120 samples per box) for a single vessel segment. Boxes labelled with NC correspond to noncalcified segments and those labelled with C to calcified ones. An

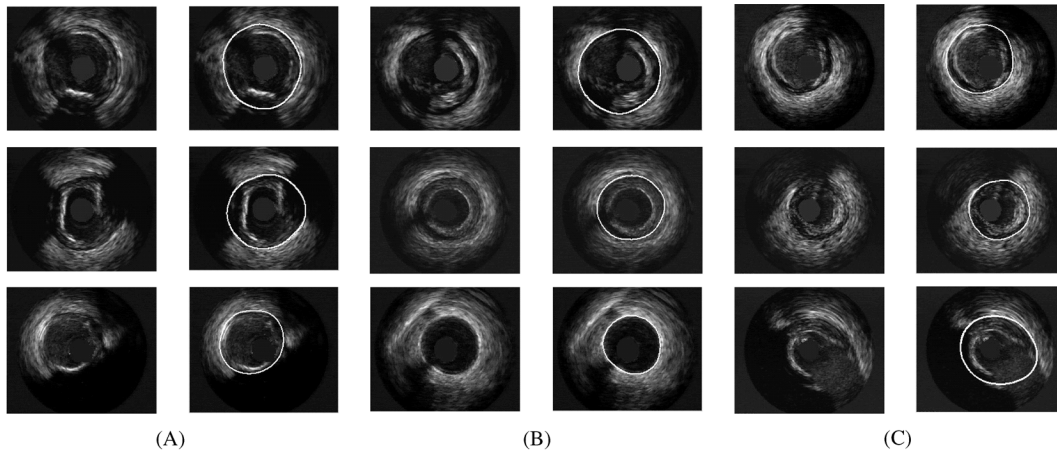


Fig. 6. Automated adventitia detections: (A) Calcified segments, (B) noncalcified plaques, and (C) uncompleted vessels.

analysis of the whisker boxes reflects robustness of segmentations: the smaller the boxes are, the more reliable the method is. In general terms, the means of automated errors are slightly higher than interobserver variability means. However, since automatic segmentation present a significantly smaller variation range than interobserver variability, our segmentation is within the experts discrepancy rate (see T-tests summary in Table I). Lack of reliable information at large angular sectors significantly increases error variability in calcified segments, both for manual and automatic segmentations.

Patients presenting an unusual large interobserver variability have been excluded, since we consider them anomalous cases with difficult and nonrobust manual identification. Frames with missing information at sectors larger than 90° have also been excluded as manual measurements are not robust either [37] and, thus, they might yield outlying error values. The statistics presented have been computed on 20 of the 22 segments available, excluding about 15% of the frames. Table II summarizes the statistical ranges for automatic errors (AUT) and interobserver variability (INT-OBS) computed for the four expert contours. A summary of the results of the T-tests comparing the total interobserver variability and automatic errors averages are given in Table I.

According to a two-tailed T-test, there is no significant difference between interobserver and automated mean absolute distance errors and difference in areas. For mean distance errors the p -value equals $p = 0.17$ and the confidence interval for the true difference in means at a significance level of 95% is $CI = (-0.002, 0.014)$. In the case of percentage in area difference, $p = 0.153404$ and the interval (also at a significance level of 95%) is $CI = (-0.017, 0.114)$. Maximum errors for automated detections are slightly above the range of maximum interobserver variability. In order to robustly determine the fraction of increase, we use a single-tailed T-test to check if the null hypothesis statement “the mean of automated maximum errors is above λ times the mean of maximum interobserver variabilities” is true. The true proportion between maximum automated error and interobserver variability is between the minimum λ rejecting the null hypothesis and the maximum accepting it. For $\lambda = 1.102$, the null hypothesis was accepted

with a p -value, $p = 0.053$, and for $\lambda = 1.103$, it was rejected with $p = 0.049$. We conclude that the increase in maximum automated errors is under 10.3%. Finally, a T-test on the mean of the automated signed distance error shows that in average it is zero as the p -value equals $p = 0.212$ and the confidence interval for the true mean is a tiny interval containing the zero value $CI = (-0.002, 0.011)$.

VIII. DISCUSSION

The combination of *a priori* knowledge (classification techniques) with filtering techniques based on continuity of image geometry is the key point for a robust characterization of vessel (the adventitia layer, in our case) borders. The reliability of the proposed strategy is reflected in the global statistics extracted from *in vivo* sequences segmentation. The fact that mean distances and vessel areas compare to interobserver variation in the case of less than 90° of missing information validates our method for extraction of clinical measurements. Since there is no bias in automated segmentations (the mean signed distance is statistically zero), we can ensure that our method achieves an optimal compromise among expert criteria as automatically traced curves lie between the curves traced by different observers. Still, the striking increase in the error range for the anomalous cases NC5 and C3 needs to be analyzed. Such misdetections correspond to vessel segments that either the adventitia is hardly identified or there is a severe lack of valid information.

Weak visual appearance of the adventitia border is a technical limitation of the ultrasound acquisition technique and it is a main cause of disagreement among experts [case C2 in Fig. 7(b)] in 9% of the cases. Our strategy suffers this kind of error in 18% of the segments under study [boxes NC5, C2, and C3 in Fig. 7(a)]. We argue that the only way to minimize the impact of border blurring is taking into account tissue motion periodicity along the sequence. Even for physicians, it is difficult to identify vessel borders by an analysis of still images. Often, they use cardiac periodicity in the movement of vessel structures to distinguish between tissue and other structures. We are currently assessing if adding Fourier analysis of image grey level

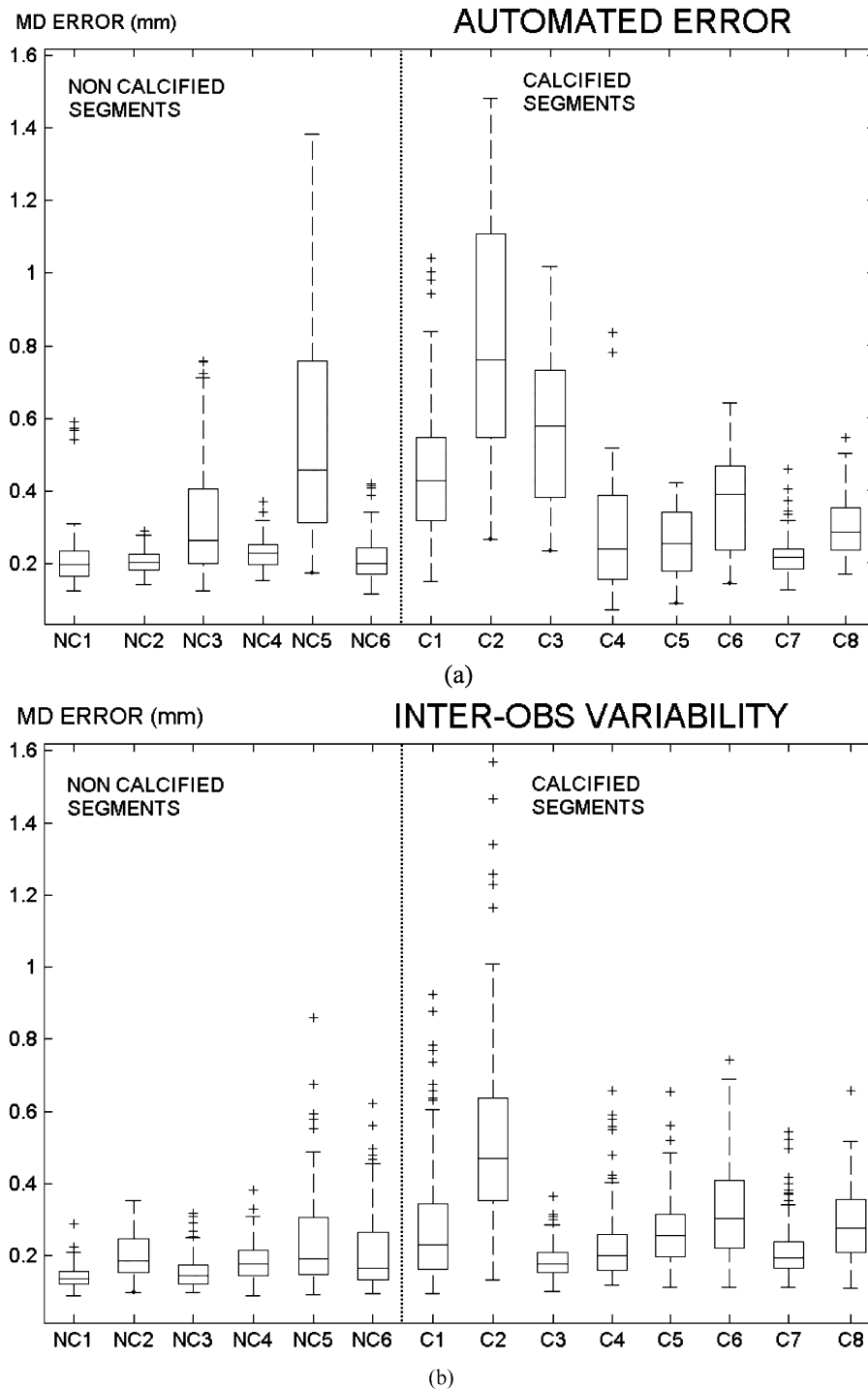


Fig. 7. Whisker boxes for (a) Aut. Error and (b) Inter-Obs. Variability.

TABLE I
STATISTICS SUMMARY ON T-TESTS COMPARING THE MEANS OF INTEROBSERVER
VARIABILITY AND AUTOMATIC ERRORS

	Confidence Interval (CI)	p-value
MeanD	(-0.002684,0.014491)	0.177721
Area Dif.	(-0.017985,0.114350)	0.153404
SgnMeanD	(-0.002401,0.010787)	0.212219

statistics to the set of adventitia descriptors reduces this type of wrong detections.

A lack of information at calcium and side branch sectors distorts measurements [37] and is a main source of error in auto-

ated models if the sparse valid information is not uniformly distributed. Images in Fig. 8 are representative of such a source of variability in manual models and show the error introduced in automated segmentations. In the first column, we show the IVUS plane [Fig. 8(a) and (f)], in the second one, the manual borders traced by two different experts [Fig. 8(b) and (g)], in the third one, ACC closure [Fig. 8(c) and (h)] and, in the last two, the B-snake model [Fig. 8(d) and (i)] and its comparison to manual borders [Fig. 8(e) and (j)]. The manual models significantly differ at those sectors where either echo shadowing (second and third quartiles in Fig. 8(b) and (g), respectively) or

TABLE II
PERFORMANCE EVALUATION OF THE ADVENTITIA SEGMENTATION STRATEGY. AUTOMATIC ERRORS VERSUS INTEROBSERVER VARIABILITY

	NON-CALCIFIED		CALCIFIED		TOTAL	
	INT-OBS	AUT	INT-OBS	AUT	INT-OBS	AUT
MaxD (mm)	0.4208 ± 0.1794	0.4238 ± 0.1026	0.6627 ± 0.3610	0.7161 ± 0.2532	0.5386 ± 0.3075	0.5715 ± 0.2296
RelMaxD (%)	0.3963 ± 0.1788	0.3868 ± 0.1075	0.5469 ± 0.3171	0.6116 ± 0.2665	0.4697 ± 0.2664	0.5122 ± 0.2344
MeanD (mm)	0.1783 ± 0.0698	0.1864 ± 0.0364	0.2650 ± 0.1306	0.2885 ± 0.0947	0.2206 ± 0.1126	0.2265 ± 0.0688
RelMeanD (%)	0.1647 ± 0.0668	0.1684 ± 0.0387	0.2142 ± 0.1113	0.2388 ± 0.0931	0.1888 ± 0.0945	0.1972 ± 0.0662
Area Dif. (%)	6.6799 ± 3.1579	7.2571 ± 1.9842	9.3511 ± 5.7529	10.0428 ± 4.0390	7.9813 ± 4.7962	8.6032 ± 3.3436
SgnMeanD (mm)	0.0004 ± 0.0769	0.0283 ± 0.0540	0.0163 ± 0.1213	-0.0381 ± 0.0912	0.0081 ± 0.1013	0.0041 ± 0.0801

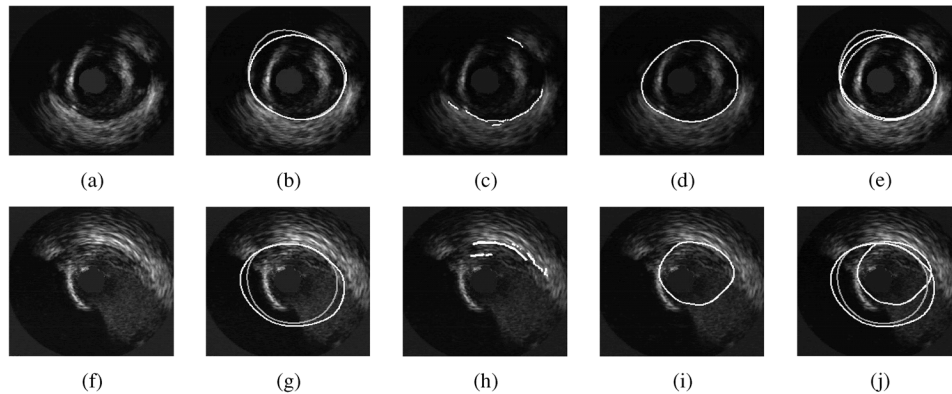


Fig. 8. Adventitia models in images with sparse information. (a), (f) IVUS images, (b), (g) manual models, (c), (h) ACC, (d), (i) final snake, and (e), (j) comparison to manual models.

blood [fourth quartile in Fig. 8(g)] hide the adventitia border, which invalidates them for any reliable measurements. In the case of automated detections, models extracted from frames with uniformly distributed information [Fig. 8(d)] adjust to reference contours [Fig. 8(e)] although their error is prone to increase due to the higher disagreement among experts. Meanwhile, in the case of having all available information gathered in one of the image quadrants, the automated model [Fig. 8(j)] accuracy drastically drops [Fig. 8(j)].

Although clinical studies [37] suggest that, under the former situation, measurements should not be reported, our studies prompt that by enforcing stronger 3-D continuity to the B-snake model, the impact of such artifacts could be reduced. Since the use of 2-D spline surfaces (NURBS) might be computationally unfeasible (by their handling of sequence blocks over 1200 frames), we suggest using the contours detected at the last frame with information available in more than three image quadrants.

IX. CONCLUSION

Vessel border detection is of special interest for plaque assessment and quantification of lumen narrowing in IVUS sequences. By its weak appearance, there are few algorithms addressing segmentation of the external adventitia border. In this paper, we propose a general strategy for vessel border detection in IVUS images with an explicit application to the segmentation of the medial-adventitial border.

The reported methodology combines classification techniques with advanced smoothing operators based on image level sets continuity. The strategy for media-adventitia detection is a three-step algorithm. We show that using geometric knowledge of image structures suffices to detect the adventitia

without precise and exhaustive classification of vessel tissue. In addition, our segmenting strategy is robust against a large variety of vessel cases, such as presence of different plaques, side branches, IVUS artifacts (echo shadowing, sensor guide), and lost of information.

The strategy has been tested on 5400 images including calcified and noncalcified vessel segments, side branches, and the most representative shadowing artifacts of IVUS sequences. The comparison to borders manually traced by four experts shows that we are within the range of interobserver variability in those images where manual measurements are reliable. We also report an exhaustive analysis of the main sources of error increase as well as possible lines of research to minimize their impact.

REFERENCES

- [1] D. Hausmann, A.J.S. Lundkvist, G. Friedrich, K. Sudhir, P.J. Fitzgerald, and P.G. Yock, "Lumen and plaque shape in atherosclerotic coronary arteries assessed by in vivo intracoronary ultrasound," *Amer. J. Cardiol.*, vol. 74, no. 9, pp. 857–863, 1994.
- [2] J. Dijkstra, G. Koning, J.C. Tuinenburg, P.V. Oemrawsingh, and J.H.G. Reiber, "Automatic border detection in intravascular ultrasound images for quantitative measurements of the vessel, lumen and stent parameters," *CARS 2001*, ser. Int. Congress 1230, pp. 916–922, 2001.
- [3] C. von Birgelen, C. D. Mario, W. Li, J. C. Schuurbiens, C. J. Slager, P. J. de Feyter, J. R. Roelandt, and P. W. Serruys, "Morphometric analysis in three-dimensional intracoronary ultrasound: An in vitro and in vivo study performed with a novel system for the contour detection of lumen and plaque," *Amer. Heart J.*, vol. 132, pp. 516–527, 1996.
- [4] C. von Birgelen, G. S. Mintz, A. Nicosia, D. P. Foley, W. J. van der Giessen, N. Bruining, S. G. Airian, J. R. T. C. Roelandt, P. J. de Feyter, and P. W. Serruys, "Electrocardiogram-gated intravascular ultrasound image acquisition after coronary stent deployment facilitates on-line three-dimensional reconstruction and automated lumen quantification," *J. Amer. Coll. Cardiol.*, vol. 30, pp. 436–443, 1997.
- [5] P.A. Brathwaite, K.B. Chandran, D.D. McPherson, and E.L. Dove, "Lumen detection in human IVUS images using region-growing," in *IEEE Proc. CiC 1996*, 1996, pp. 37–40.

- [6] Z. Luo, Y. Wang, and W. Wang, "Estimating coronary artery lumen area with optimization-based contour detection," *IEEE Trans. Med. Imag.*, vol. 22, no. 4, 2003.
- [7] E. Brusseau, C.L. de Korte, F. Mastik, J. Schaar, and A. F. W. van der Steen, "Fully automatic luminal contour segmentation in intracoronary ultrasound imaging a statistical approach," *IEEE Trans. Med. Imag.*, vol. 23, no. 5, pp. 554–566, 2004.
- [8] M. Sonka and X. Sonka, "Segmentation of intravascular ultrasound images: A knowledge based approach," *IEEE Trans. Med. Imag.*, vol. 14, no. 4, pp. 719–732, Dec. 1995.
- [9] C. Haas, H. Ermert, S. Holt, P. Grewe, A. Machraoui, and J. Barmeyer, "Segmentation of 3D intravascular ultrasonic images based on a random field model," *Ultrasound Med. Biol.*, vol. 26, no. 2, pp. 297–306, 2000.
- [10] M. E. Olszewski, A. Wahle, S. C. Mitchell, and M. Sonka, "Segmentation of intravascular ultrasound images: A machine learning approach mimicking human vision," *CARS*, pp. 1045–1049, 2004.
- [11] M. E. Olszewski, A. Wahle, S. C. Vigmostad, and M. Sonka, "Multidimensional segmentation of coronary intravascular ultrasound images using knowledge-based methods," *Proc. SPIE, Med. Imaging*, vol. 5746, no. 26, pp. 496–504, 2005.
- [12] X. Zhang and M. Sonka, "Tissue characterization in intravascular ultrasound images," *IEEE Trans. Med. Imag.*, vol. 17, no. 6, pp. 889–899, Dec. 1998.
- [13] O. Pujol and P. Radeva, "Supervised texture classification for intravascular tissue characterization," in *Handbook of Medical Image Analysis: Advanced Segmentation and Registration Models*. Norwell, MA: Kluwer, 2004.
- [14] A. Takagi, K. Hibi, X. Zhang, T. J. Teo, H. N. Bonneau, P. G. Yock, and P. J. Fitzgerald, "Automated contour detection for high-frequency IVUS imaging: A technique with blood noise reduction for edge enhancement," *Ultrasound Med. Biol.*, vol. 26, no. 6, pp. 1033–1041, 2000.
- [15] M.E. Plissiti, D.I. Fotiadis, L.K. Michalis, and G.E. Bozios, "An automated method for lumen and media-adventitia border detection in a sequence of IVUS frames," *IEEE Trans. Inf. Technol. Biomed.*, vol. 8, no. 2, pp. 131–141, Jun. 2004.
- [16] J.D. Klingensmith, R. Shekhar, and D.G. Vince, "Evaluation of three-dimensional segmentation algorithms for the identification of luminal and medial-adventitial borders in intravascular ultrasound," *IEEE Trans. Med. Imag.*, vol. 19, no. 10, pp. 996–1011, Oct. 2000.
- [17] J.D. Klingensmith, P. Schoenhagen, A. Tajaddini, S.S. Halliburton, E.M. Tuzcu, S.E. Nissen, and D.G. Vince, "Automated three-dimensional assessment of coronary artery anatomy with intravascular ultrasound scanning," *Amer. Heart J.*, vol. 145, no. 5, pp. 795–805, 2003.
- [18] J. Dijkstra, G. Koning, and J.H.C. Reiber, "Quantitative measurements in IVUS images," *Int. J. Cardiovascular Imaging*, vol. 15, no. 6, pp. 513–522, 1999.
- [19] A. Hernandez, D. Gil, P. Radeva, and E. Nofrerias, "Anisotropic processing of image structures for adventitia detection in IVUS images," in *IEEE Proc. CiC 2004*, 2004, vol. 31, pp. 229–232.
- [20] A. Hernández and D. Gil, "A Deterministic-Statistical Strategy for Adventitia Segmentation in IVUS images Aug. 2005, CVC Tech. Rep. 89 [Online]. Available: <http://cvc.uab.es/aura/>.
- [21] W.F. Young and S. McLaughlin, "Pseudo-inverse filtering of IVUS images," in *IEEE Proc. Science, Meas. and Tech.*, 1998, vol. 145, no. 6, pp. 321–326.
- [22] M. Rosales and P. Radeva, "Simulation model of intravascular ultrasound images," in *Med. Imag. Comp. Computer-Assisted Inter. (MICCAI 2004)*, 2004, LNCS (3217), Springer-Verlag, pp. 200–207.
- [23] X.M. Pardo, P. Radeva, and D. Cabello, "Discrimant snakes for 3D reconstruction of anatomical organs," *Med. Imag. Anal.*, vol. 7, pp. 293–310, 2003.
- [24] F. Vilario and P. Radeva, "Cardiac segmentation with discriminant active contours," *Artif. Intell. Res. Devel.*, IOS Press, pp. 211–215, 2003.
- [25] M. Kass, A. Witkin, and D. Terzopoulos, "Snakes: Active contour models," *Int. J. Comp. Vision*, vol. 1, no. 4, pp. 321–331, 1987.
- [26] M. Brelj and M. Sonka, "Object localization and border detection criteria design in edge-based image segmentation: Automated learning from examples," *IEEE Trans. Med. Imag.*, vol. 19, no. 10, pp. 973–985, Oct. 2000.
- [27] V. Caselles, R. Kimmel, and G. Sapiro, "Geodesic active contours," *Int. J. Comp. Vision*, vol. 22, no. 1, pp. 61–79, 1997.
- [28] D. Gil and P. Radeva, "Extending anisotropic operators to recover smooth shapes," *Comput. Vis. Imag. Under.*, vol. 99, pp. 110–125, 2005.
- [29] D. Gil, "Geometric Differential Operators for Shape Modelling," Ph.D. Thesis, Universitat Autònoma de Barcelona, Barcelona, Spain, 2004 [Online]. Available: <http://www.cvc.uab.es/debora/>
- [30] R. Carmona and S. Zhong, "Adaptative smoothing respecting feature directions," *IEEE Trans. Image Process.*, vol. 7, no. 3, pp. 353–358, 1998.
- [31] J. Weickert, *Scale-Space Theory in Computer Vision*, LNCS (1252), B. ter Haar Romeny, L. Florack, J. Koenderink, and M. Viergever, Eds. New York: Springer-Verlag, 1997, pp. 3–28.
- [32] R. Duda and P. Hart, *Pattern Classification*. New York: Wiley-Interscience, 2001.
- [33] L.C. Evans, "Partial differential equations," *Berkeley Math. Lect. Notes*, 1993.
- [34] B. Jähne, "Spatio-temporal image processing," in *Lecture Notes in Computer Science*. Berlin, Germany: Springer-Verlag, 1993.
- [35] D. R. Martin, C. C. Fowlkes, and J. Malik, "Learning to detect natural image boundaries using local brightness, color and texture cues," *IEEE Trans. Pattern Anal. Mach. Intell.*, vol. 26, no. 5, pp. 530–549, May 2004.
- [36] J.R. Landis and G.G. Koch, "The measurement of observer agreement for categorical data," *Biometrics*, vol. 33, pp. 159–74, 1977.
- [37] G.S. Mintz, "Clinical expert consensus document on standards for acquisition, measurement and reporting of intravascular ultrasound studies (IVUS)," *J. Amer. Coll. Cardiol.*, vol. 37, no. 5, pp. 1478–92, 2001.